A multiscale crater function model for ion-induced pattern formation in silicon



2009 J. Phys.: Condens. Matter 21 224018

(http://iopscience.iop.org/0953-8984/21/22/224018)

J. Phys.: Condens. Matter **21** (2009) 224018 (9pp) doi:10.1088/0953-8984/21/22/224018

# A multiscale crater function model for ion-induced pattern formation in silicon

**N Kalyanasundaram**[1], **J B Freund**[1,2] **and H T Johnson**[1]

[1] Department of Mechanical Science and Engineering, University of Illinois at Urbana-Champaign, USA
[2] Department of Aerospace Engineering, University of Illinois at Urbana-Champaign, USA

Received 8 January 2009
Published 12 May 2009
Online at stacks.iop.org/JPhysCM/21/224018

**Abstract**

The ion-induced formation of nanometer-scale ripples on semiconductors, long known as the sputter erosion surface instability, is explained using a coupled atomistic-continuum framework. Molecular dynamics simulations of individual medium energy ion impacts on an amorphous silicon target show that the average effect of an incident ion is to leave an ångström-scale crater-like impression on the surface, complete with a crater rim. The summation of many such impacts on a micron-scale surface, combined with the smoothing effect of surface diffusion, leads to the formation of surface ripples aligned perpendicular to the projected ion beam direction. The same numerical approach can be used to evaluate the standard analytical model for this process, known as the Bradley–Harper model. Both Bradley–Harper surface evolution and the atomistically determined crater function surface evolution are computed over time under conditions similar to those for known experimental data. The results show that the surface mass rearrangement associated with the finite atomistic crater rims explains a key experimental observation, ripple amplitude saturation, which cannot be accurately explained using the Bradley–Harper model or any other known numerical or analytical model for the sputter erosion surface instability.

(Some figures in this article are in colour only in the electronic version)

## 1. Introduction

Regular, quasi-periodic structures or patterns are formed on a wide variety of solids like semiconductors, metals and oxides by ion bombardment at a wide range of experimental conditions [1]. On semiconductor surfaces of interest like silicon and germanium, these surface patterns are nanometer-scale structures, typically with a peak-to-valley amplitude between 0 and 10 nm and a periodicity between 30 and 300 nm [2–5]. In experiments, the solid surfaces are often nominally flat before ion bombardment by a nearly homogeneous ion beam [6]. For this reason, the quasi-periodic nanometer-scale structures are often called self-organized nanostructures. The patterns are created by the ion-surface interactions and due to processes like surface diffusion and viscous flow that occur at or near the surface [6, 7].

### *1.1. Experimental observations*

In pattern formation studies, commonly varied experimental conditions include (i) beam incidence angle, (ii) target temperature, (iii) ion flux and fluence, and (iv) ion beam energy [8]. Other factors that are thought to influence surface evolution include surface crystallinity/structure, surface chemistry [9] and beam divergence [8].

Ripple formation has been observed on some materials at a wide range of incidence angles. In the case of silicon targets, it is typically observed between 0° and 30° off-normal beam incidence angles [5, 10] at less than 2 keV energy ranges. In GaAs, ripple formation has been observed between 30° and 60° beam angles. In other materials like $SiO_2$, Cu and InP, the formation of ripples or dots has been documented in the 0°–75° ranges [4, 11–15, 7].

Experimental observations on semiconductors and metals suggest two temperature regimes that give rise to two different ripple characteristics. At low temperatures (typically $T < 200\,^{\circ}\mathrm{C}$), the ripple wavelength is observed to be independent of temperature for both amorphous and crystalline materials; whereas, at high temperatures ($T > 200\,^{\circ}\mathrm{C}$), the ripple wavelength follows an Arrhenius law, either $\exp(-\frac{E}{2k_BT})$ or $\exp(-\frac{E}{4k_BT})$, suggesting a thermally activated

 

mechanism. Currently, the temperature dependence of the ripple wavelength is best understood in the higher temperature regime. Bradley and Harper suggest $\exp(-\frac{E}{2k_BT})$ due to a surface diffusion based smoothing effect, while Erlebacher and Aziz suggest $\exp(-\frac{E}{4k_BT})$ due to an additional effect of adatom migration/annihilation mechanism [16, 2]. In the low temperature regime, a variety of mechanisms have been suggested to explain the temperature independence of ripple wavelength [7, 8]. Some of these mechanisms include nonlinear effects such as ion-induced surface diffusion, a mechanism that depends only on the ion beam and target properties like ion range and straggle [6, 8, 17].

The effect of flux dependence has also been studied extensively in the literature [8, 16, 18]. The typical flux ranges that are considered in the experiments range from $10^{13}$ to $10^{16}$ ions cm$^{-2}$ s$^{-1}$ and the total fluences that are considered are in the range $10^{15}$–$10^{18}$ ions cm$^{-2}$. The roughness (peak-to-valley amplitude of the patterns) is known to increase as the square of the flux. The roughness is also known to increase at low fluences and saturate at higher fluences [5, 2]. The ripple wavelength is reported to be independent of ion flux in most of the studies [6, 16]; however, a systematic decrease in ripple wavelength with increasing ion flux has also been reported [8, 16].

Other beam characteristics like ion beam energy or beam divergence are also known to influence the ripple wavelength. It has been reported that the ripple wavelength increases linearly with increasing ion energies [19]. The effect of crystalline and amorphous interfaces on pattern formation have also been studied widely [20]. Pattern formation mechanisms in crystalline materials are affected by mechanisms such as anisotropic diffusivity [15], the effect of step surfaces and the Ehrlich–Schwöebel mechanism [21]. In amorphous materials, a viscous flow migration of defects has also been suggested [22, 3, 10]. Surface chemistry and strain is also known to affect pattern characteristics [9].

An increase in random roughness of the surface due to ion bombardment, called kinetic roughening, has been observed on targets like graphite [23], silicon [5], and germanium [24]. No periodic patterns are observed before or after the random roughening of the surface. The experimental conditions like temperature or beam incidence angles determine whether surface patterns are created or if the surface randomly roughens. The mechanisms that lead to kinetic roughening have been studied very widely [25, 26], especially in the context of surface evolution due to ion bombardment [8]. The section 1.2 presents a summary of the conventional theories of surface evolution. In subsequent sections we introduce and discuss a new multiscale method, called the crater function method, to study surface evolution. The crater function method does not assume the development of surface patterns or a randomly rough surface due to bombardment and, in principle is capable of explaining observations of both ripple formation and randomly rough surfaces.

### *1.2. Existing theories for surface evolution*

Conventional theories of pattern formation can be classified into three main categories: (i) theories that explain pattern formation, (ii) theories that explain kinetic roughening and (iii) theories that explain both pattern formation and kinetic roughening in a single framework. In this section, conventional pattern formation theories and their shortcomings are discussed first. Conventional kinetic roughening theories are discussed next. Combined theories, usually nonlinear and/or stochastic extensions to the pattern formation theories, are described subsequently.

Bradley and Harper formulate the first continuum theory describing the formation of self-organized patterns [6]. According to the Bradley–Harper theory, which is a deterministic and linear formulation, ion bombardment roughens the surface by an incidence angle-dependent sputtering. This roughening is countered by surface diffusion.

Ion impacts on a target surface energize atoms and create a collision cascade resulting in displacement of atoms away from their equilibrium positions [20]. The incoming atom loses energy to target atoms and will come to rest when the kinetic energy of the incoming atom is less than the potential energy barriers [27]. Some atoms at the surface may receive sufficient energy to overcome the surface binding energy and sputter.

During a collision cascade, the energy transferred to the target atoms may result in the creation of vacancies and recoils if the target atoms are displaced far enough from their equilibrium positions. When the ion and the atom energies are sufficient, the mean distances over which successive events occur are greater than interatomic distances; the collision cascade created by such displacements is then said to be linear [20]. Using a Boltzmann transport equation approach, Sigmund formulates a sputtering theory that describes the shape and size of a collisional cascade. In Sigmund's sputtering theory, the collisional volume and the shape of the constant energy contours in a linear cascade regime are described as ellipsoids centered at the penetration depth. The ellipsoid's major axis is directed along the ion beam direction. The number of atoms sputtered is related to the shape and size of the collisional volume. As the incident direction changes, the major axis changes; therefore, the collisional volume and the constant energy contours change. This, as a result, leads to variation of sputter yield with changing incidence angle. The range of slopes of ripple structures observed experimentally is small (typically less than 5°–10°). Using a first-order expansion of sputter yield with respect to surface slopes, Bradley and Harper first show that erosion rate is directly proportional to surface curvature due to the variation in the density of collisional ellipsoids with curvature in the linear cascade regime.

The physical processes during ion bombardment on an initially flat surface are described by Bradley and Harper as follows. The surface erosion rate $\mathbf{r} = (\mathbf{x}, h(\mathbf{x}, t))$, where $\mathbf{x} = (x_1, x_2)$ represents spatial coordinates in a coordinate frame as defined in figure 1 (with $x_1$ along the projected direction of the ion beam) and $t$ represents time, is proportional to the total energy available at that surface point due all ion impacts. Note that figure 1 also shows a schematic of the differences between an effective local angle $\theta$ and a global beam angle $\phi_{\text{beam}}$.

Using Sigmund's sputtering theory, the energy available at any point at $\mathbf{r}$ due to an impact at $(\mathbf{x}_0, h(\mathbf{x}_0, t))$, where

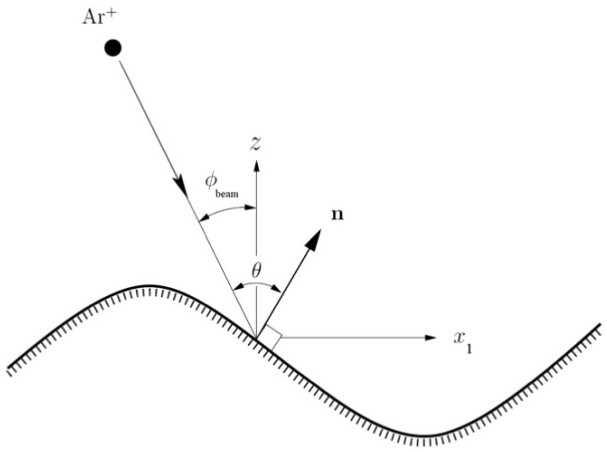


**Figure 1.** Schematic of the global beam angle and the local surface angle for an ion arriving at the surface.

$\mathbf{x}_0 = (x_{01}, x_{02})$, is described by a Gaussian distribution function so that

$$E(\mathbf{r}) = \frac{\varepsilon}{(2\pi)^{\frac{3}{2}}\sigma\mu^2} \times \exp\left[-\frac{(h-h_0-a_P)^2}{2\sigma^2} - \frac{(x_1-x_{01})^2+(x_2-x_{02})^2}{2\mu^2}\right] \quad (1)$$

where $E(\mathbf{r})$ is the total energy available due to the ion impact at $\mathbf{r} = (\mathbf{x}, h(\mathbf{x}, t))$, $\mathbf{x} = (x_1, x_2)$, $h = h(\mathbf{x}, t)$, $h_0 = h(\mathbf{x}_0, t)$, $\varepsilon$ is the energy of an incident ion, $a_P$ is the penetration depth and $\sigma$ and $\mu$ represent material-dependent properties of the constant energy ellipsoids, as shown in figure 2. Due to the assumption that the erosion rate at any arbitrary point on the surface is proportional to the sum total of energy available at that point due to impact all impacts on the surface, the erosion rate is calculated using the integral of energy available at the surface due to an impact:

$$\frac{\partial h}{\partial t} \propto \int\int \mathrm{d}\mathbf{r}\, E(\mathbf{r})\Phi(\mathbf{r}) \quad (2)$$

where $\Phi(\mathbf{r})$ is a geometric correction to the uniform flux $J$ due to surface curvature.

A simplified expression obtained by linear expansion of (2) describing the surface height at time $t$, or $h(\mathbf{x}, t)$, is

$$\frac{\partial h}{\partial t} = S_1(\theta)\frac{\partial^2 h}{\partial x_1^2} + S_2(\theta)\frac{\partial^2 h}{\partial x_2^2} - B\nabla^2\nabla^2 h \quad (3)$$

where $\mathbf{S}(\theta) = (S_1(\theta), S_2(\theta))$ is proportional to the slope-dependent sputter yield, the flux, and the area of the target. $B$ is the surface diffusion coefficient given by $B = D_s C\gamma/n^2 k_B T$ where $\gamma$ is the surface energy density, $k_B$ is the Boltzmann constant, $T$ is the temperature, $D_s$ is the surface diffusivity and $C$ is the concentration of mobile species which take part in the surface diffusion. By linear stability analysis, it can be shown that a dominant wavelength $\lambda_{max}$ manifests itself as surface ripples at large times and is given by

$$\lambda_{max} = \sqrt{\frac{2B}{S(\theta)}} \quad (4)$$

where $\mathbf{S}(\theta) = \max(S_1(\theta), S_2(\theta))$. If $S_1(\theta) > S_2(\theta)$, then the ripples are oriented along the 1-direction; otherwise, they are oriented along the 2-direction.

Bradley and Harper attempt to explain experimental observations of ripple rotation within the framework described above. In the experiments, at near normal incidences the ripples are oriented perpendicular to the projected ion beam. At large angles off-normal, ripples are oriented parallel to the projected ion beam direction. Bradley and Harper explain that at near normal incidence angles, $S_1(\theta) > S_2(\theta)$. Therefore, the ripples are oriented along the 1-direction (perpendicular to the projected direction of the ion beam). However, as $\theta$ increases, $S_1(\theta)$ decreases and $S_2(\theta)$ increases. At large angles off-normal, $S_1(\theta) < S_2(\theta)$. This causes the ripples to rotate to be oriented along the 2-direction.

Experimental studies of the temperature scaling of ripple wavelengths correlate well with predictions using the Bradley and Harper mechanism in high temperature experiments [8, 16, 2]. However, not all experimental observations can be explained using this mechanism [8, 15, 21, 22, 3, 10]. Many theories, some introducing stochastic terms to equation (3), some accounting for the inherent nonlinearities in

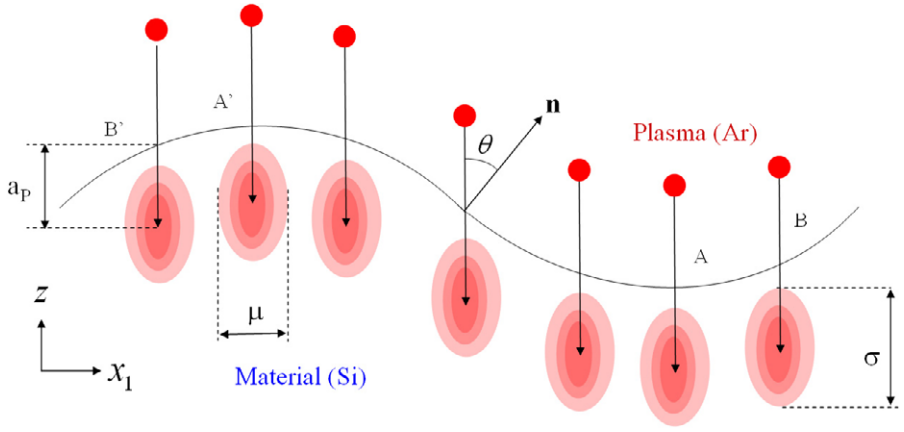


**Figure 2.** Schematic of the Gaussian ellipsoids used in the Bradley–Harper approach. According to the Bradley–Harper mechanism, the change in height at any point on the surface is proportional to the total energy that is available at that point due to all impacts.

the problem, and some introducing both stochastic and nonlinear terms have been proposed to explain phenomena like amplitude saturation of ripples [28, 29, 8, 27]. Various modifications to the $\mathbf{S}(\theta)$ or an effective/modified $B$ have been proposed to account for shadowing and ballistic transport effects [29, 30, 27, 28]. All of these theories and corrections explain the growth rate or the temperature dependence of $\lambda_{\max}$ using a Bradley–Harper-like framework based on the theory of sputtering. Despite the success in applying the Bradley–Harper theory and its modifications to many pattern formation experiments, the theory still fails to predict certain observations made in many of the cited experiments. The shortcomings of the theory can be directly explained to be due to the exclusive use of Sigmund's sputtering theory—thereby neglecting mass rearrangement—and also due to the assumption that surface height change is proportional to the net energy deposited by the ion.

The evolution equations that describe kinetic roughening due to ion bombardment are usually either a modification of the Kardar–Parisi–Zhang equation [25] or a modification of the Kuramoto–Sivashinsky equation [8]. The Kardar–Parisi–Zhang equation is given by

$$\frac{\partial h}{\partial t} = \nu_{x_1}\frac{\partial^2 h}{\partial x_1^2} + \nu_{x_2}\frac{\partial^2 h}{\partial x_2^2} + \frac{l_1}{2}\left(\frac{\partial h}{\partial x_1}\right)^2 + \frac{l_2}{2}\left(\frac{\partial h}{\partial x_2}\right)^2 + \eta(x,t) \tag{5}$$

where $\nu_{x1}$, $\nu_{x2}$, $l_1$, and $l_2$ are constant coefficients that determine the asymptotic scaling laws of the randomly rough surfaces. The signs of $l_1$ and $l_2$ determine whether the surface roughness increases according to a power-law scaling or logarithmic scaling of some characteristic length. The $\eta(\mathbf{x}, t)$ term is a stochastic addition that models the random arrival of ions at $\mathbf{x}$.

One representation of the Kuramoto–Sivashinsky (KS) equation, called the noisy KS equation [28], is given by

$$\frac{\partial h}{\partial t} = \nu\nabla^2 h - K\nabla^4 h + \eta(x,t) \tag{6}$$

where $\nu$ and $K$ are constants that determine the scaling of the surface roughness. The KS equation has been used to interpret kinetic roughening in some ion bombardment experiments [23, 31]. Despite the similarity between the KS equation and the Bradley–Harper equation, the KS equation cannot predict pattern formation because the coefficient of the second derivatives of surface heights in the KS equation, $\nu$, is negative (8) whereas in (3), $\mathbf{S}(\theta)$ is positive. The KS or the KPZ equations alone fail to predict pattern formation that is observed in many ion bombardment experiments. Therefore, the kinetic roughening theories alone are insufficient to describe surface evolution by ion bombardment.

Many theories that can predict both pattern formation and kinetic roughening have been proposed. These theories are invariably nonlinear and stochastic extensions to the Bradley–Harper mechanism. For example, the evolution equation from Cuerno's unified theory is given as

$$\frac{\partial h}{\partial t} = S_1(\theta)\frac{\partial^2 h}{\partial x_1^2} + S_2(\theta)\frac{\partial^2 h}{\partial x_2^2} - B\nabla^2\nabla^2 h + \frac{l_1}{2}\left(\frac{\partial h}{\partial x_1}\right)^2 + \frac{l_2}{2}\left(\frac{\partial h}{\partial x_2}\right)^2 + \eta(x,t) \tag{7}$$

where $S_1(\theta)$, $S_2(\theta)$, $l_1$, $l_2$, and $K$ are constants. The $\eta(\mathbf{x}, t)$ term models the random arrival of the ion at the surface. By sweeping over all possible parameter-space for the constants mentioned above, parameter regimes that separately describe pattern formation or kinetic roughening are determined in these theories. The unified theories make assumptions similar to the Bradley–Harper theory; for example, the surface erosion rate due to bombardment is assumed proportional to a Gaussian energy deposition. Therefore, the unified theories have shortcomings similar to the Bradley–Harper mechanism. The nonlinearity allows explanation of some additional features of surface amplitude evolution that cannot be explained by the Bradley–Harper mechanism. For example, these theories predict that surface amplitude saturates at long times; however, the predicted saturation amplitude is at least an order of magnitude higher than what is observed in experiments.

Due to the shortcomings associated with existing pattern formation theories, a direct simulation method is presented in this work. The new method proposed here is capable of predicting both pattern formation and kinetic roughening. The direct simulation method includes both sputtering and rearrangement and does not make assumptions on the relation between evolution rate and the shape and size of collisional cascades.

## 2. Multiscale modeling method

The predictive capacity of the existing surface evolution models that use Bradley–Harper like approaches is improved here by incorporating the actual effects of individual ion impacts into a new multiscale model. These ion impact effects can be computed atomistically and are referred to as crater functions. Details of the calculation of crater functions for ion-bombarded silicon are presented in an earlier paper [32].

The multiscale simulation method has two stages: the first stage computes an average response of the target surface to an impact, called the crater function; the second uses the crater functions along with the thermally activated surface diffusion equation to evolve micrometer-scale surfaces over long times. This separation of timescales is justified since a single ion impact at typical experimental fluxes changes surface heights over timescales of a few nanoseconds and length scales of a few nanometers. Surface diffusion, on the other hand, occurs at much larger length and timescales. Since these two effects change the surface heights at such disparate length and timescales, it is convenient to treat individual ion impacts to be separate and independent from surface diffusion.

The evolution of the surface is thus governed by

$$\frac{\partial h}{\partial t} = g\left(\mathbf{x}, \theta\left(\mathbf{x}\right), t\right) - B\nabla^2\nabla^2 h, \tag{8}$$

where $B\nabla^2\nabla^2 h$ is the diffusive smoothing and $g(\mathbf{x}, \theta(\mathbf{x}), t)$ is the net roughening due to ion bombardment. This equation can be used to track surface evolution in the manner of the Bradley–Harper governing equation (3), but by using our crater functions to compute $g(\mathbf{x}, \theta(\mathbf{x}), t)$, it is possible to avoid making assumptions about the shape of the collision cascade and the relation of erosion rate to energy deposition.

In previous work, simulations of silicon surface evolution due to argon impacts are presented [32]. These simulations use crater functions computed by molecular dynamics (MD). We note that the multiscale method developed here can still be used to predict Bradley–Harper like growth rates if crater functions relevant to the Bradley–Harper like mechanisms are available. For example, in considering only Sigmund sputtering, the proportionality of erosion rate to Gaussian energy deposition implies that the crater functions are Gaussian functions. Using Gaussian functions in the multiscale method developed here should still predict amplitude evolution as observed in Bradley–Harper like theories. The crater functions may also be found directly from experiments for some combinations of ion, target and beam properties. For example, it is possible to observe the shape of craters due to single cluster impacts on surfaces [33]. The average crater shapes in these experiments are the appropriate crater functions. Furthermore, it is possible to alter the crater functions computed from MD or sputtering theory and study surface evolution using these modified crater functions. Studying surface evolution using modified crater functions may provide insight into the effects of the MD craters and into new mechanisms of surface evolution.

Since ion bombardment is fundamentally a discrete process and one must numerically integrate equation (8) in time to study surface evolution, it is most convenient to construct a model in discrete form. First, if the impacts are independent of each other, then $g(\mathbf{x}, \theta(\mathbf{x}), t) = fA\Delta h_{\text{ion}}(\mathbf{x} - \mathbf{x}_0^i, \theta(\mathbf{x}_0))$ where $f$ is the ion flux and $A$ is the projected surface area of the target and the average response at $\mathbf{x}$ relative to $\mathbf{x}_0$ is called the impact crater function: $\Delta h_{\text{ion}}(\mathbf{x} - \mathbf{x}_0^i, \theta(\mathbf{x}_0))$. The change in $h$ over time $\Delta t$ is given by

$$h(\mathbf{x}, t + \Delta t) = h(\mathbf{x}, t) + \sum_{i=1}^{N_r} \Delta h_{\text{ion}}\left(\mathbf{x} - \mathbf{x}_0^i, \theta\left(\mathbf{x}_0^i\right)\right) + \Delta h_{\text{diff}}, \tag{9}$$

where $N_r$ is the number of random impacts on the simulated $L_x \times L_y$ surface in time $\Delta t$ and $\mathbf{x}_0^i$ are the $N_r$ random impact points.

For simulations presented here, $L_{x1} = L_{x2} = 1.011\ \mu$m. It is assumed that the $N_r$ consecutive impacts that occur within each $\Delta t$ do not interact directly. A typical number of impacts per $\Delta t$ time step is $5 \times 10^5$, and it can be shown that results with impact numbers per time step of up to and greater than this number are identical. By carrying out the simulation over multiple $\Delta t$ time steps, an experimentally measurable number of ion impacts, typically more than $10^{10}$ on the $1.011\ \mu$m $\times$ $1.011\ \mu$m surface, can be simulated.

The argument $\theta(\mathbf{x}_0)$ in the average crater function is the effective local angle of incidence in $\Delta h_{\text{ion}}(\mathbf{x} - \mathbf{x}_0^i, \theta(\mathbf{x}_0))$, which parameterizes how the shape of the crater depends on the slope at the impact point. If an ion is incident on a flat surface with zero slope in all directions, then $\theta(\mathbf{x}_0)$ is same as the beam angle $\phi_{\text{beam}}$. When an ion is incident at a beam angle $\phi_{\text{beam}}$, with a projected direction along the $x_1$ axis, on a surface patch that can be described by slopes $m_1$ and $m_2$ in the $x_1$ and $x_2$ directions respectively around the impact point, the effective local angle of incidence is given by

$$\theta(\mathbf{x}_0) = \arccos\left(\frac{m_1 \sin(\phi_{\text{beam}}) + \cos(\phi_{\text{beam}})}{\sqrt{1 + m_1^2 + m_2^2}}\right). \tag{10}$$

The surface has an initial random roughness of 1 Å and is discretized with $2048 \times 2048$ collocation points. Any grid point $(i, j)$ has an associated $\mathbf{x} = (x_1, x_2)$ Cartesian coordinate and a surface height denoted by $h_{i,j}(t) = h(\mathbf{x}, t)$ at time $t$, and any grid point $(i, j)$ can be an impact point.

The slopes $m_1$ and $m_2$ are calculated using a central difference scheme about the point of impact. If the impact coordinate indices are given by $(i, j)$, then

$$m_1 = \frac{h_{i+1,j} - h_{i-1,j}}{2\Delta x_1} \quad \text{and} \quad m_2 = \frac{h_{i,j+1} - h_{i,j-1}}{2\Delta x_2}. \tag{11}$$

After the surface is updated due to the $N_r$ random ion impacts simulated by individual crater functions at the appropriate local angles, the change due to surface diffusion, $\Delta h_{\text{diff}}$, is solved over time $\Delta t$. The discrete Fourier transform of $h(\mathbf{x}, t)$ to $\hat{h}(\mathbf{k}, t)$ is first carried out, where $\mathbf{k} = (k_1, k_2)$. This gives

$$\Delta\hat{h}_{\text{diff}}(\mathbf{k}, t + \Delta t) = \hat{h}_{\text{diff}}(\mathbf{k}, t) \times \left(\exp\left[-B\Delta t\left(k_1^2 + k_2^2\right)^2\right] - 1\right). \tag{12}$$

To ensure isotropy despite the square domain, after each $\Delta t$ the $h$ field is filtered such that $\hat{h} = 0$ for $|\mathbf{k}| > \frac{2\pi N}{L}$, where $L = 1.011\ \mu$m and $N = 2048$. The results can be shown to be independent of $\Delta t$. The algorithm can also be validated against analytic results by carrying out the surface evolution analysis with $B = 0$ and a functional form of $g(\mathbf{x}, \theta(\mathbf{x}), t)$ such that an analytical solution can be obtained; the surface diffusion part of the evolution equation admits an exact solution, so that the only error is due to computing the finite spectrum.

## 3. Results

Crater functions averaged from at least 500 ensembles for each of a range of incidence angles ($\theta = 0°, 4°, 8°, 12°, 16°, 20°, 24°, 28°$) [32], along with the numerical surface diffusion analysis, are used to study surface evolution of a micrometer-sized silicon target. An ion flux of $10^{15}$ ions cm$^{-2}$ s$^{-1}$ is used in the simulations. Again, when an ion is incident on the surface, it changes the local surface height and, therefore, it changes the effective local incidence angles for subsequent arriving ions. An appropriate crater function corresponding to the local ion incidence angle is used to increment the surface height after each impact. The crater functions are available only for the set of discrete angles listed above; however, the effective local incidence angle can be any real value. An appropriate crater function is calculated by interpolating the available crater functions using piecewise cubic splines in $\theta(\mathbf{x})$. At large angles, a linear runout boundary condition is used in calculating the spline coefficients. In order to ensure the projected direction of the ion beam used on micron-sized surfaces is aligned along the projected direction of the ion

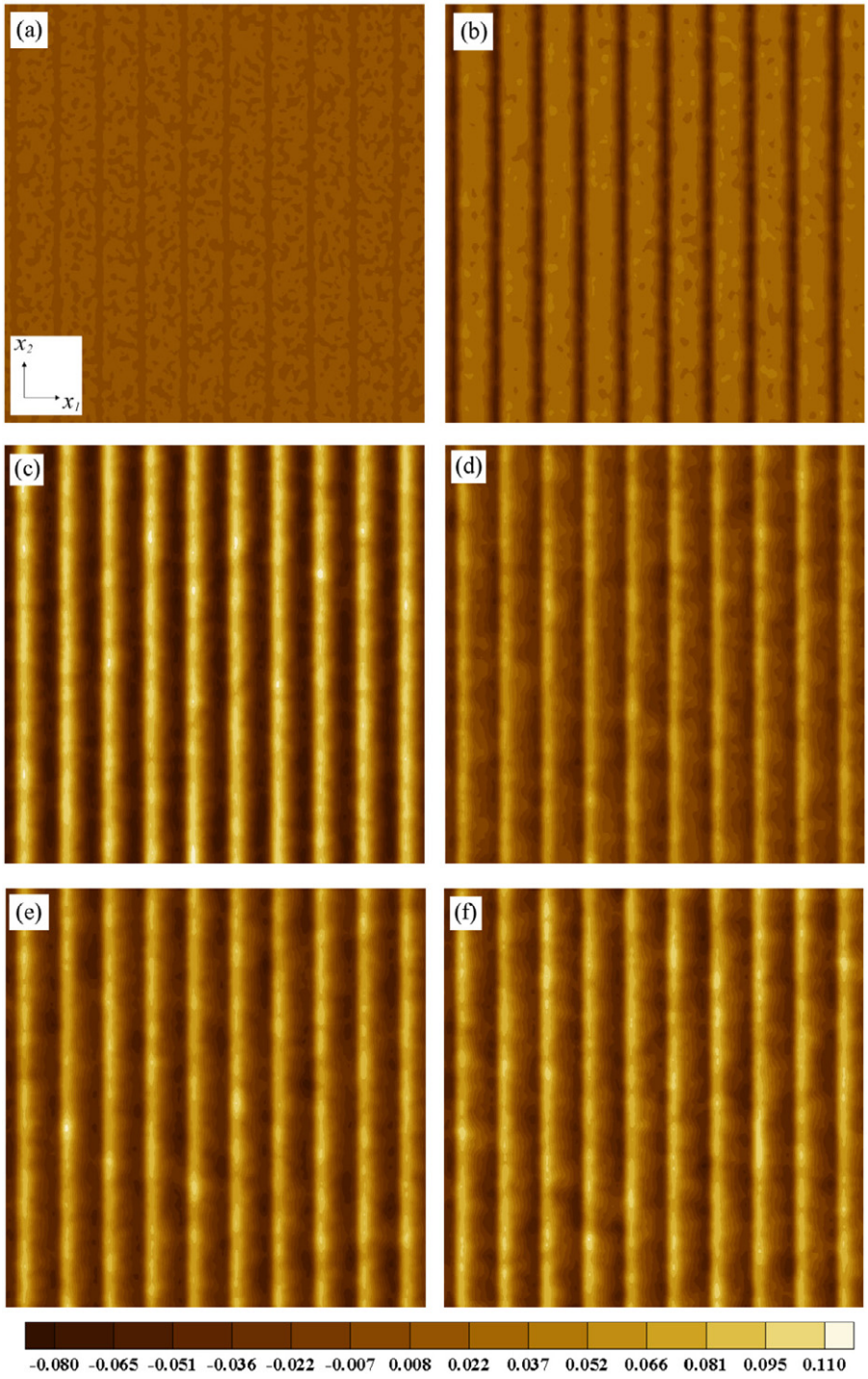


**Figure 3.** Formation of nanometer-scale surface structures (ripples) on silicon. Surface structure for $B = 5.684 \times 10^{-34}$ m$^4$ s$^{-1}$ at nondimensional times $t^* =$ (a) 0.496, (b) 1.241, (c) 6.207, (d) 12.414, (e) 18.621 and (f) 24.828. The projected direction of the 15° incident ion beam is along the $x_1$ direction. The shading shows surface height in nondimensional units.

beam used in the MD simulations, the crater functions are rotated in the plane before incrementing the surface height. After rotation, the crater functions are mapped to the computational grid using bicubic interpolation.

Time and height are nondimensionalized as $t^* = tB(\frac{2\pi}{\lambda})^4$ and $h^* = h\frac{2\pi}{\lambda}$, respectively, where $h$ is half the peak-to-valley height. For the conditions that are simulated in this work, the silicon surface evolves into a rippled nanometer-scale surface pattern. Nanometer-scale structures obtained using this method are shown in figure 3 at six different nondimensional times for $B = 5.684 \times 10^{34}$ s$^{-1}$, which is similar to the diffusivity deduced by Erlebacher [2] for a silicon surface. The structure observed in figure 3(f) corresponds to 20 billion ion impacts on the initially unpatterned surface, with $N_r = 50\,000$. The maximum nondimensional amplitudes of these structures are about 0.1. The orientation of ripples

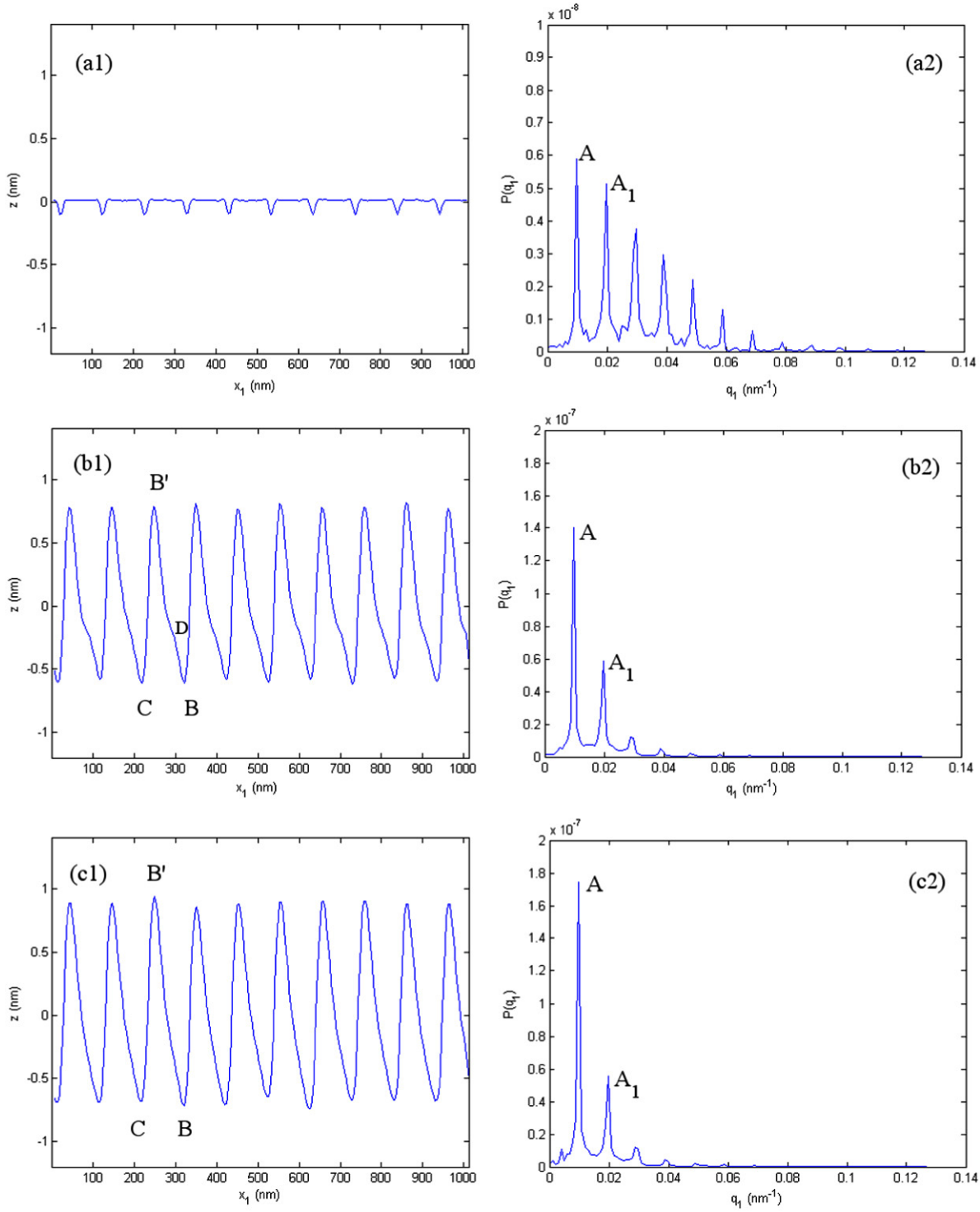


**Figure 4.** Rippled surface structures formed on silicon and their power spectrum: surface structure averaged along the $x_2$ direction and its power spectrum is shown at nondimensional times $t^* =$ ((a1), (a2)) 1.241, ((b1), (b2)) 12.414 and ((c1), (c2)) 24.828. The peak marked as A in the power spectrum corresponds to the dominant wavenumber and peak $A_1$ corresponds to the second dominant wavenumber.

is approximately perpendicular to the projected ion beam direction. The amplitude of the two-dimensional structure when averaged in the $x_2$ direction is shown in figure 4 for three nondimensional times along with the FFT power spectrum for each ripple. Further, the two faces of any ripple shown in figure 4 are observed to be asymmetric. A magnified view of one of the ripples at time $t^* = 24.828$ is shown in figure 5. The magnitude of the ripple slope of the B′B face measured when $h = 0$ is smaller (3°) than that of the B′C face (6°). Therefore, the maximum effective local angle of incidence on the B′B face is 18° and on the B′C face is 9° for a 15° beam incidence angle. The differences in the slopes of B′B and B′C faces are not due to shadowing because shadowing effects are not explicitly taken into account. The difference in the slopes is due to

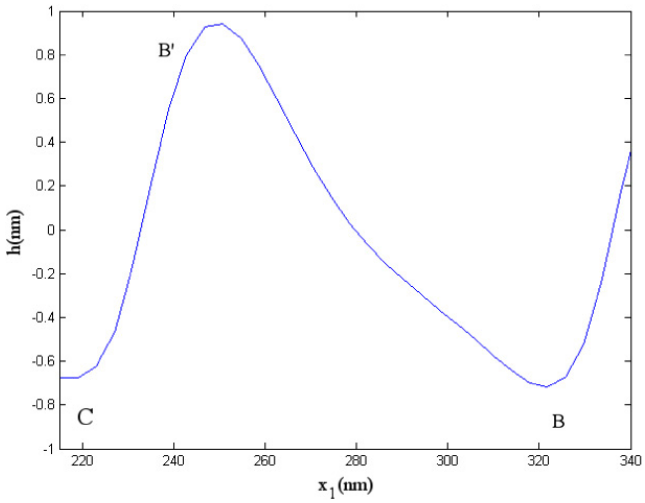


**Figure 5.** Magnified view of the rippled surface structure averaged along the $x_2$ direction at nondimensional time $t^* = 24.828$. The magnitude of ripples slope on the B′B face when $h = 0$ is smaller than that on the B′C face.

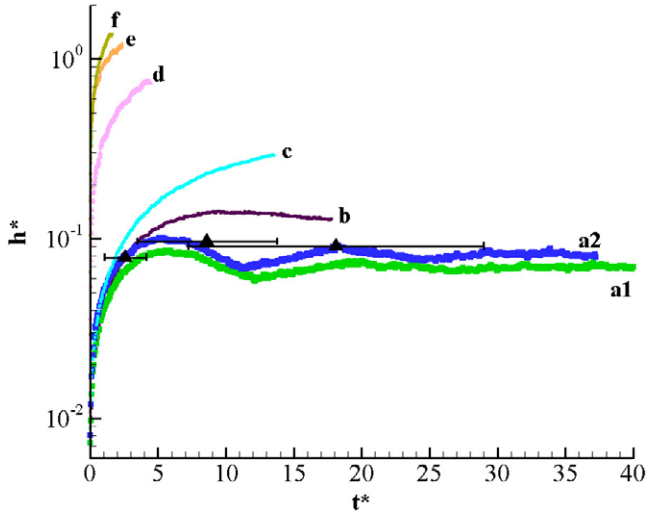


**Figure 6.** Surface height evolution: ((a)–(f)) simulation results; black triangles: experimental data [5]. The simulation results are based on ($a_1$) MD crater function with $B = 5.684 \times 10^{-34}$ m$^4$ s$^{-1}$; ($a_2$) actual crater function with $B = 9.094 \times 10^{-34}$ m$^4$ s$^{-1}$; (b) 15° crater functions for all impacts, (c) normal incidence crater function for all impacts, (d) Gaussian crater functions with crater volumes equal to volume of sputtered atoms only, (e) Gaussian crater function (GCF) matching the depth (0.701 Å) and width of the normal incidence crater functions, and (f) computed crater functions with rims removed. The triangles represent the experimental scaled times and saturated amplitudes; the error bars represent the variation due to uncertainty of diffusion coefficients in the experiments.

the bombardment of the steep face (B′C) at lower effective incidence angles than the BC face. From the crater functions, it is observed that the downstream driven mass rearrangement, or downhill mass current, is reduced at lower incidence angles. Thus, the differences in the crater functions used for the B′B and B′C faces could lead to differences in the slopes of the two faces. In figures 4(a2), (b2) and (c2), the peak in the power spectrum marked A represents the dominant wavevector and the peak marked $A_1$ has the second largest contribution to the power spectrum. It is observed that the wavelength of the ripple is set at very low fluences (early times) and that the wavelength does not change with increasing fluence.

The amplitude of these ripples increases very rapidly at low fluences and saturates at large fluences. Figure 6 shows the evolution of the nondimensional amplitude of the nanometer-scale structures as a function of nondimensional time. The $h^*$ are plotted in figure 6 for different diffusion coefficients along with data obtained for argon bombardment of silicon by Ziberi *et al*. The beam energy used in this study (500 eV) and incidence angle (15°) are within the range of experimental values reported by Ziberi *et al*. However, because $B$ is not reported for the experiments, the dimensionless $h^*$ and $t^*$ are calculated using a range of $B$ values from $B = 4 \times 10^{-4}$ to $10 \times 10^{-34}$ m$^4$ s$^{-1}$, in a similar range as the simulations. The calculated growth rates and saturation amplitudes match well with experiments. Figure 6 (curves $a_1$ and $a_2$) shows agreement with Ziberi *et al* at the same incidence angle; the saturation amplitude is also similar to that observed by Erlebacher (2) at larger impact angles.

Earlier theories predict saturation amplitude at an order of magnitude larger than experimentally observed, or they predict no saturation at all [6, 29, 2]. Amplitude saturation has been explained previously using nonlinear expansions [34]. However, in the present work, we link the accurate prediction of the saturation amplitude to a microscopic mechanism associated with mass rearrangement. As incidence angles increase, the MD crater functions show increasingly preferential atom movement in the downstream direction. This acts as a smoothing mechanism in the form of a downhill mass flux, preferentially filling in the valleys and smoothing peaks of any features, causing the peak-to-valley amplitude to diminish. However, as the peak-to-valley amplitude diminishes, the effective local angle of incidence at various impact points diminishes. At lower angles, near the beam angles considered here, the mass rearrangement is reduced. Thus, reduced amplitude is associated with roughening of the surface, and increasing of the peak-to-valley amplitude. A balance between the roughening mechanisms and the mass rearrangement driven smoothing mechanisms would cause amplitudes to saturate.

Using Gaussian crater functions without rims, as in Sigmund's sputtering model which does not account for mass rearrangement or pile-up in the form of crater rims, leads to an increase in surface amplitudes larger than experimentally observed surface amplitudes (figure 6, curves d and e). Figure 6(d) shows the amplitude growth when the Gaussian crater volume corresponds to volume of sputtered atoms only. However, using no-rim Gaussian crater functions with craters as large as the actual craters that account for both sputtering and rearrangement, we observe a faster growth rate. Using a normal incidence crater function for all impacts, that is, ignoring the local incidence angle $\theta$, leads to a slower growth rate compared to the Gaussian case because of the presence of a small crater rim in the normal incidence crater function (figure 6, curve c). If we use the 15° crater function for all

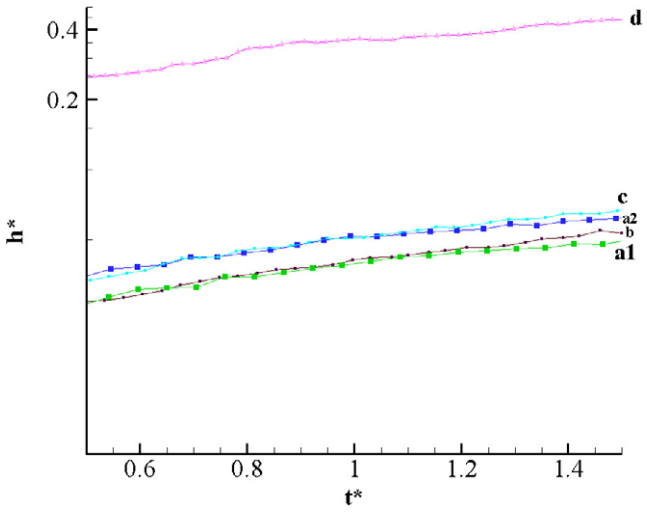


**Figure 7.** Surface height evolution at small times. This figure is a magnified view of figure 4 for a smaller range of times. The crater functions used to generate curves a–d are noted in figure 6. The exponential growth rates for the different cases are: (a1) 0.514, (a2) 0.544, (b) 0.665, (c) 0.732, and (d) 0.596.

impacts, saturation is observed (figure 6, curve b). This is possibly due to the asymmetric crater rims creating downhill mass movement that increases with increasing incidence angles.

Artificially removing the crater rim completely from all the computed crater functions leads to the highest growth rate observed (figure 6, curve f). This result is expected because such a crater function not only has deep craters, but also scoops out material preferentially from the downstream direction compared to the upstream direction. Such a preferential material removal mechanism would cause the ripple structures to grow steeper by removing material from the region of large slope (like regions near a saddle point between a peak and a valley). In the cases without asymmetric rims, amplitude saturation is not observed. Figure 7 shows a magnified view of figure 6 for a smaller range of times. As seen from figure 7, the exponential growth rates associated with the MD crater functions and the Gaussian crater functions with crater volumes equal to the volume of sputtered atoms are similar at small times. The Bradley–Harper theory (Gaussian crater functions) is known to predict the experimentally observed growth rates at small times correctly [2, 35]; however, at large fluences, either no saturation is observed (in linear theories) or saturation is observed at an amplitude higher than experimental amplitudes (in nonlinear theories) [2].

## 4. Summary and conclusions

In summary, a new computational method is developed to use ion impact crater functions along with diffusion modeling via a continuum model; the approach, which can be validated against known analytical solutions, is used to study mechanisms of surface evolution under low-to-medium energy ion bombardment.

In particular, for bombardment of Si with 500 eV Ar ions at temperatures low enough to preclude annealing, it is found that the average ion impact causes a deep crater, significantly deeper than expected from sputter erosion alone, surrounded by a crater rim that becomes increasingly asymmetric for impact angles further from normal. The crater functions are computed by averaging over thousands of ensembles of MD simulations of surface height change due to an ion impact.

Incorporation of these crater functions into a continuum model that includes surface diffusion reproduces the types of surface structures observed in experiments better than previous models based on consideration of sputtering, but not other mechanisms of mass rearrangement. The asymmetry of the crater rims leads to amplitude saturation in agreement with that observed experimentally.

## Acknowledgments

We gratefully acknowledge the support of NSF grants CMS 05-10624 and CMMI 08-25173.

## References

[1] Cahill D G 2003 *J. Vac. Sci. Technol.* A **21** S110
[2] Erlebacher J *et al* 2000 *J. Vac. Sci. Technol.* A **18** 115
[3] Chason E *et al* 1994 *Phys. Rev. Lett.* **72** 3040
[4] Chan W L and Chason E 2005 *Phys. Rev.* B **72** 165418
[5] Ziberi B *et al* 2005 *Phys. Rev.* B **72** 235310
[6] Bradley R M and Harper J M E 1988 *Phys. Rev.* **94** 262
[7] Mayer T M, Chason E and Howard A J 1994 *J. Appl. Phys.* **76** 1633
[8] Makeev M A, Cuerno R and Barabasi A-L 2002 *Nucl. Instrum. Methods Phys. Res.* B **197** 185
[9] Ozaydin G *et al* 2007 *Nucl. Instrum. Methods Phys. Res.* B **264** 47–54
[10] Ziberi B, Frost F and Rauschenbach B 2006 *J. Vac. Sci. Technol.* A **24** 1344
[11] Shulga V 2001 *Nucl. Instrum. Methods Phys. Res.* B **174** 423
[12] Hu X, Cahill D G and Averback R S 2000 *Appl. Phys. Lett.* **76** 3125
[13] Fackso S *et al* 1999 *Science* **285** 1551
[14] Frost F, Schindler A and Bigl F 2000 *Phys. Rev. Lett.* **85** 4116
[15] Rusponi S, Boragno C and Valbusa U 1997 *Phys. Rev. Lett.* **78** 2795
[16] Erlebacher J *et al* 1999 *Phys. Rev. Lett.* **82** 2330
[17] Ozaydin G *et al* 2005 *Appl. Phys. Lett.* **87** 163104
[18] Liu Z X and Alkemade P F A 2001 *Appl. Phys. Lett.* **79** 4334–6
[19] Umbach C C, Headrick R L and Chang K C 2001 *Phys. Rev. Lett.* **87** 246104
[20] Sigmund P 1969 *Phys. Rev.* **184** 383
[21] Rusponi S *et al* 1998 *Phys. Rev. Lett.* **81** 2735
[22] Volkert C 1991 *J. Appl. Phys.* **70** 3521
[23] Ecklund E A *et al* 1991 *Phys. Rev. Lett.* **67** 1759
[24] Chason E *et al* 1998 *J. Vac. Sci. Technol.* **B7** 332–6
[25] Kardar M, Parisi G and Zhang Y C 1986 *Phys. Rev. Lett.* **56** 889
[26] Edwards S F and Wilkinson D R 1982 *Proc. R. Soc.* A **381** 17
[27] Carter G and Vishnyakov V 1996 *Phys. Rev.* B **54** 17647
[28] Cuerno R and Barabasi A-L 1995 *Phys. Rev. Lett.* **74** 4746
[29] Makeev M A and Barabasi A-L 1997 *Appl. Phys. Lett.* **71** 2800
[30] Moseler M *et al* 2005 *Science* **309** 1545
[31] Ecklund E A, Snyder E J and Williams R S 1993 *Surf. Sci.* **285** 157
[32] Kalyanasundaram N *et al* 2008 *Appl. Phys. Lett.* **92** 131909
[33] Birtcher R C *et al* 2008 *Nucl. Instrum. Methods Phys. Res.* B **206** 851–4
[34] Park S *et al* 1999 *Phys. Rev. Lett.* **83** 3486
[35] Chason E, Chan W L and Barathi M S 2006 *Phys. Rev.* B **74** 224103